Model, Analysis, and Design of a q-Axis Self-Synchronizing Current Control for Three-Phase Grid-Connected Converters

Eliabe D. Queiroz, *Member, IEEE*, João I. Y. Ota, and José Antenor Pomilio, *Senior Member, IEEE*

***Abstract*—This article introduces a q-axis self-synchronizing current control strategy for three-phase grid-connected converters with *LCL* filters, encompassing its modeling, analysis, and design. Grid-forming converters synchronize with the grid by adjusting terminal voltage magnitude and frequency based on deviations in active and reactive power references. In contrast, grid-following converters use a phase-locked loop for synchronization, where a controller regulates output current by commanding the converter voltage. Building on these concepts, the proposed strategy achieves self-synchronization by monitoring deviations from current references and dynamically adjusting the amplitude and frequency of the synthesized voltage. This method enables a self-synchronizing current control that achieves grid synchronization independently of grid voltage measurements. Real-time hardware-in-the-loop testing validates the effectiveness of the q-axis self-synchronizing control. It also demonstrates the accuracy of the linearized model in representing system dynamics. The control strategy maintains stable operation under both ideal and nonideal grid conditions. Furthermore, this article provides a root-locus analysis of the linearized state-space model, a detailed design methodology, and a comprehensive stability analysis, including the impact of the operating point on system dynamics. Practical aspects such as a start-up procedure and an *LCL* reactive power compensation method are also addressed to support real-world implementation.**

***Index Terms*—Converter stability, eigenvalue stability, grid-connected converter, hardware-in-loop simulation, self-synchronizing control.**

Nomenclature

C_c	LCL filter capacitance.
f_{sw}	Switching frequency.
f_s	Sampling frequency.
$\mathbf{I}_{n\times n}$	Identity matrix of n order.
$\mathbf{J}$	$= \begin{bmatrix} 0 & -1 \\ 1 & 0 \end{bmatrix}$; coupling between d- and q-axis.
$\mathbf{i}_{abc,o}$	Output current in the abc-frame.
$\mathbf{i}^c_{dq,o}$	Output current in the CRF.
$i^c_{d,o}$	Output current in the d-axis of the CRF.
$i^c_{q,o}$	Output current in the q-axis of the CRF.
$\mathbf{i}^m_{dq,o}$	Output current in the MRF.
$i^m_{q,o}$	Output current in the q-axis of the MRF.
$\mathbf{i}^c_{dq,\text{ref}}$	Reference of current in the CRF.
$i^c_{d,\text{ref}}$	Reference of current for the d-axis of the CRF.
$i^c_{q,\text{ref}}$	Reference of current for the q-axis of the CRF.
K_{AQ}	Damping gain of the q-axis self-synchronizing loop.
K_D	Proportional constant of the d-axis loop.
K_Q	Proportional constant of the d-axis self-synchronizing loop.
L_{eq}	LCL filter equivalent inductance.
L_{ci}	LCL filter internal inductance.
L_{co}	LCL filter external inductance.
P_n	Nominal active power.
p_o	Active power output.
P_{ref}	Reference of active power.
q_o	Reactive power output.
Q_{ref}	Reference of reactive power.
R_{eq}	LCL filter equivalent resistance.
R_{ci}	LCL filter internal resistance.
R_{co}	LCL filter external resistance.
R_d	LCL passive damping resistance.
S_n	Nominal apparent power.
T_D	Time constant of the d-axis loop.
T_Q	Time constant of the q-axis self-synchronizing loop.
T_s	Sampling period.
$\mathbf{v}_{abc,i}$	Converter voltage in the abc-frame.
$\mathbf{v}^c_{dq,i}$	Converter voltage in the CRF.
$v^c_{d,i}$	Converter voltage in the d-axis of the CRF.
$v^c_{q,i}$	Converter voltage in the q-axis of the CRF.
$\mathbf{v}_{abc,g}$	Grid voltage in the abc-frame.
$v^c_{q,g}$	Grid voltage in the q-axis of the CRF.
$\mathbf{v}^m_{dq,g}$	Grid voltage in the MRF.
$v^m_{d,g}$	Grid voltage in the d-axis of the MRF.
$v^m_{q,g}$	Grid voltage in the q-axis of the MRF.
V_{dc}	DC-link voltage.
V_{rms}	RMS nominal line voltage.

Received 7 June 2024; revised 18 October 2024 and 28 January 2025; accepted 23 February 2025. Date of publication 6 March 2025; date of current version 14 April 2025. This work was supported in part by the National Council for Scientific and Technological Development (CNPq), under Grant #141997/2017-6 and Grant #303859/2020-2, in part by the São Paulo Research Foundation (FAPESP), under Grant #2016/08645-9, and in part by the Electricity Sector Research and Development Program under Grant PD-00063-3058/2019-PA3058: "MERGE - Microgrids for Efficient, Reliable and Greener Energy," regulated by the National Electricity Agency (ANEEL) in partnership with CPFL Energia (local utility). Recommended for publication by Associate Editor E. Babaei. *(Corresponding author: Eliabe D. Queiroz.)*

Eliabe D. Queiroz and José Antenor Pomilio are with the School of Electrical and Computer Engineering, Universidade Estadual de Campinas, Rua Albert Einstein 400, Brazil (e-mail: eliabe@unicamp.br; antenor@unicamp.br).

João I. Y. Ota is with Hitachi Energy Sweden AB, 721 83 Västerås, Sweden (e-mail: jiyota@unicamp.br).

Color versions of one or more figures in this article are available at https://doi.org/10.1109/TPEL.2025.3548550.

Digital Object Identifier 10.1109/TPEL.2025.3548550

V_0	Peak nominal voltage.
$\boldsymbol{\xi}^c_{dq,o}$	Integral of current errors in the CRF.
$\xi^c_{d,o}$	Integral of current error in the d-axis of the CRF.
$\xi^c_{q,o}$	Integral of current error in the q-axis of the CRF.
Ω_0	Nominal frequency.
Ω_{lpf}	Cut-off frequency of the low-pass filters.
θ_c	Angle of the CRF.
θ_m	Angle of the MRF.
ϕ_c	Phase angle difference between CRF and MRF.
$\mathbf{T}_{dq,abc}$	Transformation from the abc- to dq-frame.
$\mathbf{T}_{\alpha\beta,abc}$	Transformation from the abc- to $\alpha\beta$-frame.
$\mathbf{R}(\phi_c)$	$= \begin{bmatrix} \cos(\phi_c) & \sin(\phi_c) \\ -\sin(\phi_c) & \cos(\phi_c) \end{bmatrix}$; rotation matrix.
K_{id}	Proportional constant of the start-up current PLL.
T_{CT}	Waiting time for current transients.
T_{PS}	Waiting time for pre-synchronization.
ω_c	Converter frequency.
$\mathbf{R}^{\phi}(\phi_c)$	$= \frac{d\mathbf{R}(\phi_c)}{d\phi_c}$.
ω_m	Frequency of the MRF and the grid.
$\mathbf{S}_{11}$	$= \begin{bmatrix} 1 & 0 \\ 0 & 0 \end{bmatrix}$.
$\mathbf{s}_2$	$= \begin{bmatrix} 0 & 1 \end{bmatrix}$.

I. Introduction

THREE-PHASE grid-connected converters usually consist of controllable voltage-source inverters (VSIs) connecting a dc-link-based power supply (or energy storage) to the electrical grid through an output filter (or grid-connection filter). Such a filter can either be a purely inductive filter or an LCL filter, which is the most commonly used for grid-connected converters in distribution grids [1]. The operation of such converters is based on two fundamental principles: control of the voltage or the current at the terminal of the converter and its synchronization to the electrical grid [2], [3]. For example, the synchronization process of grid-following converters [1] estimates the grid voltage angle by directly measuring the grid voltage. Phase-locked loop (PLL) and frequency-locked loop systems are examples of methods based on this synchronization principle. A synchronous reference frame (SRF) aligned to the grid voltage is the keystone to controlling the voltage or current of the grid-connected converter. Such a convention leads to the understanding that current or voltage control and synchronization tasks should be distinct.

Numerous algorithms that implement grid synchronization for grid-following converters are presented in the literature [4], [5], [6]. Nevertheless, the overall performance of the control relies on the synchronization algorithm, which is heavily affected by the power quality of the grid voltage. The current controller of the grid-following converter has a minor influence on the synchronization in a grid with low equivalent impedance at the point of common coupling (PCC). Conversely, in cases where the grid presents a high equivalent impedance at the PCC, the resulting actions of the current controller affect the voltage on the PCC, which is used by the synchronization algorithm [7], [8]. This effect due to the grid impedance may compromise the operation and stability of the grid-following converter.

However, the rationale of distinct tasks for control and synchronization is not deemed necessary for every grid-connected converter. The self-synchronizing control based on power control is seen in the grid-forming converters, where feedback loops adjust the frequency and magnitude of the terminal voltage of the grid-connected converter according to a set of variables to be controlled, which are typically the active and reactive powers [3], [9].

Grid-forming converters can also coordinate to sustain the voltage around nominal conditions. One or a group of grid-forming converters may energize a microgrid when the ac mains are lost, which is an impossible task for grid-following converters [10]. This capability is achieved in droop control and other grid-forming strategies, which adjust voltage frequency and amplitude within a limited range based on deviations in active and reactive power.

Several controls in the literature show self-synchronization capability. The "power synchronization control" (PSC) is proposed in [11] and later extended in [9], [12], and [13]. It performs grid synchronization without a PLL block by using an active power controller. This grid-forming strategy can also be modified to regulate a dc-link voltage. The "reactive PSC," reaches the grid synchronization using the reactive power exchanged to the ac mains, is presented in [14] and [15]. Although PSCs and the well-known droop control are regarded distinctively by the literature, both are similar self-synchronizing controls, and intrinsic steady-state deviations in power response exist for both strategies [16], [17].

Such grid-forming strategies lack inherent current limitation capability. When the voltage magnitude decreases, the current magnitude must increase to maintain the same active or reactive power reference, which may lead to overcurrents. Nested control loops with internal saturation can keep the current within safe limits but affect the power control capability and synchronization dynamics. Additional synchronization strategies are required to prevent loss of synchronism [12], [18].

This article proposes a self-synchronizing control based on current control for grid-connected converters. This approach stems from the conception that synchronization and control tasks can be combined. Still, it deviates from conventional PSC and droop-based control since the converter frequency is regulated employing current measurements instead of power calculations. The proposed synchronization process uses the error in the q-axis current reference to regulate frequency, including an additional proportional gain, and the error in the d-axis current reference to control the voltage magnitude. The proposed control process aims to achieve zero-error current regulation, avoiding steady-state deviations often seen in droops of power-synchronizing strategies [16], [17]. It also provides the intrinsic capability to limit the converter current, which is essential to avoid operation interruptions when grid voltage oscillates. This self-synchronizing control strategy ensures a precise power or current output that is consistent and stable.

Alqatamin et al. [19] also presented a self-synchronizing current control using observers for the grid voltage.

They demonstrate the Lyapunov stability of the system under the assumption of constant frequency and current references. Nevertheless, the model from [19] does not fully consider the impact of the angle dynamics on the transformation of currents from the *abc*-frame to the SRF, which is a critical aspect of the synchronization dynamics. This article addresses this gap by realizing a comprehensive mathematical model based on space-state equations that explore the dynamics of transformations between reference frames and the effects on the converter stability. Moreover, a methodology to design the self-synchronization current controller is developed based on the linearized model. The effects of angle dynamics are evaluated through eigenvalue analysis of the linearized model. Hardware-in-the-loop (HIL) simulations confirm both eigenvalue analysis and design. A start-up procedure for synchronization is also proposed to avoid high current values when the converter synchronizes to the grid, as well as a method to compensate for the reactive power consumed by the *LCL* filter, which are features not included in [19].

The rest of this article is organized as follows. Section II presents the notation and the definitions used for the reference frames. Section III mainly describes and models the proposed self-synchronizing current control in space-state equations and includes practical aspects of power control. Section IV shows a design methodology for the gains of the proposed self-synchronizing current control while analyzing the stability through the linearized model. Section V mainly presents the HIL verification, which consists of real-time simulation in a Typhoon HIL 604 in ideal and nonideal grids and comparisons to the linearized model. In Section V, practical aspects related to starting up the converter and operation during voltage sags are also presented. Finally, Section VI concludes this article.

II. Representation on a Common SRF

A. Notation

A common synchronous reference frame (MRF) is used to describe the dynamics of the SRF of different converters [20]. This section explains the notation because each reference frame represents the same electrical quantity or control variable differently.

First, electrical quantities and control variables on MRF and the converter synchronous reference frame (CRF) are described by the superscripts g and c, respectively. Subscripts describe the quantity either on the stationary reference frame (*abc*) or on the SRF (*dq*). Subscripts also describe if the variable is a reference, an input signal, or an output signal within the control system. For example, $i^m_{d,o}$ describes the d-axis output currents on the MRF, and $i^c_{q,\text{ref}}$ describes the q-axis reference currents on the CRF, respectively. Next, vectors always represent the quantities in a specific reference frame. For example, $\mathbf{i}^m_{dq,o} = \begin{bmatrix} i^m_{d,o} & i^m_{q,o} \end{bmatrix}^T$ are dq-frame output currents on MRF while $\mathbf{i}_{abc,o}$ are the three-phase output currents on *abc*-frame. Finally, when x is linearized, $\overline{x}$ and $\widetilde{x}$ represent its operating point and the variations around it, respectively, which yields $x = \overline{x} + \widetilde{x}$. The same notation is applied to vectors, e.g., $\mathbf{x} = \overline{\mathbf{x}} + \widetilde{\mathbf{x}}$.

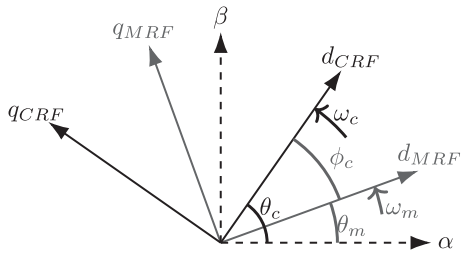

Fig. 1. Multiple reference frames in the same plane: voltage and current vectors differ among frames due to different angle positions of the frames through time.

B. Definitions

When the control is performed in an SRF, measurements taken from the three-phase values are transformed into the SRF

$$\mathbf{i}^c_{dq,o} = \mathbf{T}_{dq,abc}(\theta_c)\mathbf{i}_{abc,o} \tag{1}$$

in which, $\mathbf{T}_{dq,abc}(\theta_c) = \mathbf{R}(\theta_c)\mathbf{T}_{\alpha\beta,abc}$ is the transformation from the *abc*-frame to the *dq*-frame, and

$$\mathbf{T}_{\alpha\beta,abc} = \begin{bmatrix} \frac{2}{3} & -\frac{1}{3} & -\frac{1}{3} \\ 0 & \frac{1}{\sqrt{3}} & -\frac{1}{\sqrt{3}} \end{bmatrix}.$$

The angle position of the CRF is

$$\theta_c = \int_0^t \omega_c(\tau)d\tau + \phi_{c,0} \tag{2}$$

an integral of ω_c, the frequency of the reference frame. The constant $\phi_{c,0}$ is the initial phase angle of the CRF in $t = 0$. The matrix $\mathbf{R}(\theta_c)$ is described by

$$\mathbf{R}(\theta_c) = \begin{bmatrix} \cos(\theta_c) & \sin(\theta_c) \\ -\sin(\theta_c) & \cos(\theta_c) \end{bmatrix}. \tag{3}$$

A complete model must examine the interactions between synchronization and control so the control design aims to keep the stable operation of the grid-connected converter. An external reference frame is an effective method to observe the synchronization with the grid. Thus, a transformation to MRF is applied

$$\mathbf{i}^m_{dq,o} = \mathbf{T}_{dq,abc}(\theta_m)\mathbf{i}_{abc,o} \tag{4}$$

where $\theta_m = \int_0^t \omega_m(\tau)d\tau$ is the angle of the MRF.

Fig. 1 describes the MRF and the CRF in the $\alpha\beta$ plane. Due to the angular differences between MRF and CRF, current or voltage measurements are distinct in each reference frame. Aside from the vectors with null magnitude, every voltage or current vector is decomposed differently through time in the $\alpha\beta$-frame, the CRF, and the MRF.

A model describing the effects of CRF synchronization is essential. Here, the MRF is used as a reference to describe the circuit dynamics. This implies a frame transformation that interfaces and affects the inputs and outputs of the CRF. As a simple example, *abc*-frame current measurements transformed to the CRF are described as a transformation from MRF to CRF

$$\mathbf{i}^c_{dq,o} = \mathbf{R}(\phi_c)\mathbf{i}^m_{dq,o} \tag{5}$$

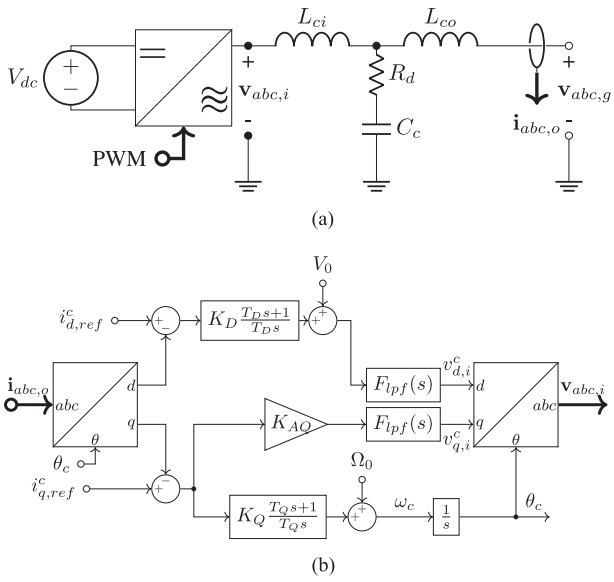

Fig. 2. Grid-connected converter. (a) Equivalent circuit of the VSI and an LCL-type filter with output current measurement. (b) Diagram of the resultant control loops for the proposed q-axis self-synchronizing current control.

where the dq-frame currents $\mathbf{i}^m_{dq,o}$ in the MRF are represented as $\mathbf{i}^c_{dq,o}$ in the CRF, and ϕ_c is the phase difference between these two reference frames, as shown in Fig. 1.

III. q-Axis Self-Synchronizing Current Control

A. Overview of the Proposed Control

Fig. 2(a) describes a three-phase grid-connected converter featuring an LCL-type filter, while Fig. 2(b) shows the proposed self-synchronizing current control with q-axis current synchronization.

Since the passband of the synchronization typically is below the grid frequency, the synchronization dynamics are much slower than the LCL resonances. Therefore, it is reasonable to assume that the LCL filter is practically inductive, leading to a simplified equivalent filter from Fig. 2(a)

$$\begin{aligned} R_{\text{eq}} &= R_{\text{ci}} + R_{\text{co}} \\ L_{\text{eq}} &= L_{\text{ci}} + L_{\text{co}}. \end{aligned} \tag{6}$$

Equation (6) is valid in the low-frequency range, which is the main focus of the studies of synchronization dynamics.

A self-synchronizing control strategy aims to ensure a smooth converter output by regulating the amplitude, phase, and frequency of $\mathbf{v}_{abc,i}$. Note that it is the transformation of $\mathbf{v}^c_{dq,i}$ to the abc-frame. Synchronization between $\mathbf{v}_{abc,i}$ and $\mathbf{v}_{abc,g}$ occurs if the dynamics between converter and grid are stable [2], [20]. The phase angle between CRF and MRF expresses the swing between the two reference frames. It is given as

$$\phi_c(t) = \theta_c(t) - \theta_m(t) = \int_0^t \Big(\omega_c(\tau) - \omega_m(\tau)\Big)\, d\tau + \phi_{c,0} \tag{7}$$

where θ_c and θ_m are the angular positions of the CRF and the MRF, respectively, ω_c and ω_m are the frequencies of the grid-connected converter and the grid, respectively, and $\phi_{c,0}$ is an initial phase angle difference.

There are two options to design a current control loop for self-synchronizing strategies:

i) to use the d-axis current for synchronization and the q-axis current for regulating the voltage magnitude;
ii) vice-versa, which is shown in Fig. 2(b).

Option (i) results in a feedback control with similar dynamics to the traditional droop control. In the traditional droop control, the self-synchronizing feedback loop regulates the active power output, which becomes less damped as the frequency droop gain increases. When it reaches a threshold value, the grid-connected converter becomes unstable [21], [22]. Option (ii) results in a feedback control with similar dynamics to the droop control for resistive lines presented in [23] and improved in [24] and [25]. In the droop control for resistive lines, the self-synchronizing feedback loop, which regulates the reactive power output, also becomes less damped as the frequency droop gain increases. However, the eigenvalues remain in the left complex plane for a wider range of droop gains [23].

The design shown in Fig. 2(b) relies solely on the current measurements, $\mathbf{i}_{abc,o}$, forming a single-loop control with greater stability compared to nested loop configurations [26]. The voltage magnitude at the converter terminal is mainly the result of the output of the d-axis current regulation of $\mathbf{i}^c_{dq,o}$. The self-synchronizing loop calculates the converter frequency from the q-axis current regulation. Fast adjustments in phase angle are implemented in the q-axis of $\mathbf{v}^c_{dq,i}$, a result of the q-axis regulation of $\mathbf{i}^c_{dq,o}$.

Depending on the converter parameters, the resonance of the LCL filter and the discretization can affect stability mainly in the high-frequency range. First-order low-pass filters (LPFs) $F_{\text{lpf}}(s)$ and a damping resistor R_d are inserted into the control loop and in the LCL filter to avoid such effects. Both are depicted in Fig. 2(a) and (b). The cut-off frequency of the LPFs is set to half of the LCL resonance. The resonance is usually 1/10 of f_{sw}, resulting in a bandwidth significantly wider than the grid frequency. In this case, the LPFs do not affect the dynamics in the low-frequency range; therefore, they are not considered in the model. Note that an LPF in the frequency loop is unnecessary, as the integral of the converter frequency that results in θ_c also attenuates fast perturbations.

B. Active and Reactive Power References

Although the self-synchronization current control does not use voltage measurements, the power flow is controllable since the converter synthesizes $\mathbf{v}_{abc,i}$. In the CRF, the active (p_o) and reactive (q_o) output powers in the grid-connected converter are obtained by

$$p_o = \frac{3}{2}\left(v^c_{d,i} i^c_{d,o} + v^c_{q,i} i^c_{q,o}\right) \tag{8}$$

$$q_o = \frac{3}{2}\left(v^c_{q,i} i^c_{d,o} - v^c_{d,i} i^c_{q,o}\right). \tag{9}$$

Considering that losses due to R_{eq} are negligible, (8) and (9) differ from the powers obtained by measuring $\mathbf{v}_{abc,g}$ due to nonidealities of the grid-connected converter and the active and reactive power absorbed by the LCL filter. Note that, in steady state, $\overline{\mathbf{v}}^c_{dq,i}$ presents only its d-axis component since $\overline{v}^c_{q,i} = 0$. Also, if $\mathbf{v}^c_{dq,i}$ is kept relatively constant, the active and reactive powers become mainly functions of the currents. Therefore, as $\mathbf{v}^c_{dq,i}$ is known, the d- and q-axis current setpoints $i^c_{d,\text{ref}}$ and $i^c_{d,\text{ref}}$ can be functions of active (P_{ref}) and reactive (Q_{ref}) power

$$i^c_{d,\text{ref}} = \frac{2P_{\text{ref}}}{3v^c_{d,i}}, \quad i^c_{q,\text{ref}} = -\frac{2Q_{\text{ref}}}{3v^c_{d,i}}. \tag{10}$$

Saturation can limit such references to avoid overcurrent. For the remainder of this work, the current references are assumed to be fixed.

C. Compensation of Reactive Power of the Output Filter

As mentioned in Section III-B, reactive power is absorbed by the LCL as current flows in the grid-connected converter terminals, resulting in a reduced power factor in cases where only active power flow is intended for the grid-connected converter.

To compensate for the reactive power absorbed by the LCL filter, the q-axis current reference in (10) is updated by adding the respective current deviation due to the reactive power offset. The eventual q-axis current reference becomes

$$i^c_{q,\text{ref}} = -\frac{2Q_{\text{ref}}}{3v^c_{d,i}} - \frac{{i^c_{d,\text{ref}}}^2 \Omega_0 L_{\text{eq}}}{\overline{v}^c_{d,i}} \tag{11}$$

where the first term on the right-hand side is the q-axis current due to the reactive power reference, and the second term on the right-hand side is the reactive power due to the LCL filter. Equation (11) excludes the capacitor reactive power since the LCL is predominately inductive around the fundamental frequency of the grid.

D. Linearized Model

The frequency of the grid-connected converter is regulated around the nominal frequency Ω_0 by utilizing the output of the controller of the q-axis current

$$\omega_c = \Omega_0 + K_Q(i^c_{q,\text{ref}} - i^c_{q,o}) + \frac{K_Q}{T_Q}\xi^c_{q,o} \tag{12}$$

where $\xi^c_{q,o}$ is the integral of the error of the q-axis current, K_Q and T_Q are the proportional gain and the time constant of the PI controller for the synchronization, respectively.

Let the integral of the errors ($\xi^c_{d,o}$ and $\xi^c_{q,o}$) to the d- and q-axis current setpoints $i^c_{d,\text{ref}}$ and $i^c_{q,\text{ref}}$ be

$$\xi^c_{d,o} = \int_0^t i^c_{d,\text{ref}} - i^c_{d,o} d\tau \tag{13}$$

$$\xi^c_{q,o} = \int_0^t i^c_{q,\text{ref}} - i^c_{q,o} d\tau. \tag{14}$$

Equation (7) describes the synchronization dynamics of the grid-connected converter, represented by the difference in phase angle between the CRF and the MRF, locked, respectively, on the voltages $\mathbf{v}^m_{dq,i}$ and $\mathbf{v}^m_{dq,g}$. Substituting (12) in (7), rearranging it to a matrix notation and including transformations of frame yields

$$\frac{d}{dt}\phi_c = \Omega_0 + K_Q \mathbf{s_2} \mathbf{i}^c_{dq,\text{ref}} - K_Q \mathbf{s_2} \mathbf{R}(\phi_c) \mathbf{i}^m_{dq,o} + \frac{K_Q}{T_Q} \mathbf{s_2} \boldsymbol{\xi}^c_{dq,o} - \omega_m \tag{15}$$

where $\mathbf{s_2} = \begin{bmatrix} 0 & 1 \end{bmatrix}$ and $\boldsymbol{\xi}^c_{dq,o} = \begin{bmatrix} \xi^c_{d,o} & \xi^c_{q,o} \end{bmatrix}^T$.

In CRF, the d-axis voltage is regulated around the nominal value V_0 by the controller of the d-axis current. While the q-axis voltage is typically set to zero, a proportional controller is added in this component. As a result, the voltages of the grid-connected converter are

$$\mathbf{v}^c_{dq,i} = \begin{bmatrix} V_0 + K_D(i^c_{d,\text{ref}} - i^c_{d,o}) + \frac{K_D}{T_D}\xi^c_{d,o} \\ K_{AQ}(i^c_{q,\text{ref}} - i^c_{q,o}) \end{bmatrix} \tag{16}$$

where K_D and T_D are the proportional gain and the time constants of the d-axis current controller, respectively, and K_{AQ} is the additional proportional gain for the q-axis current error. This gain is first proposed in this article to the authors' best knowledge and its effect is analyzed and discussed in Section V-F.

Considering the change between the MRF and CRF presented in (3), the actual currents produced by the converter voltage in (16) are

$$\frac{d}{dt}\mathbf{i}^m_{dq,o} = \frac{1}{L_{\text{eq}}}\mathbf{R}^{-1}(\phi_c)\mathbf{K}_C\left(\mathbf{i}^c_{dq,\text{ref}} - \mathbf{R}(\phi_c)\mathbf{i}^m_{dq,o}\right) + \frac{1}{L_{\text{eq}}}\mathbf{R}^{-1}(\phi_c)\left(\frac{K_D}{T_D}\mathbf{S}_{11}\boldsymbol{\xi}^c_{dq,o} + \mathbf{v}^c_{dq,i}\right) - \frac{1}{L_{\text{eq}}}\mathbf{v}^m_{dq,g} - \frac{R_{eq}}{L_{\text{eq}}}\mathbf{i}^m_{dq,o} - \mathbf{J}\omega_m\mathbf{i}^m_{dq,o} \tag{17}$$

and the behavior of the integral of the errors becomes

$$\frac{d}{dt}\boldsymbol{\xi}^c_{dq,o} = \mathbf{i}^c_{dq,\text{ref}} - \mathbf{R}\left(\phi_c\right)\mathbf{i}^m_{dq,o} \tag{18}$$

since it is also affected by the transition between reference frames.

The linearization of the system composed by (15), (17), and (18) results in the following linear state space model:

$$\begin{cases} \frac{d}{dt}\widetilde{\mathbf{x}}_{\text{ss}} = \mathbf{A}_{\text{ss}}\widetilde{\mathbf{x}}_{\text{ss}} + \mathbf{B}_{\text{ss,vg}}\widetilde{\mathbf{v}}_{dq,g} + \mathbf{B}_{\text{ss,ref}}\widetilde{\mathbf{i}}_{dq,\text{ref}} \\ \qquad\qquad + \mathbf{B}_{\text{ss},\omega g}\widetilde{\omega}_m \\ \widetilde{\mathbf{y}}_{\text{ss}} = \mathbf{C}_{\text{ss}}\widetilde{\mathbf{x}}_{\text{ss}} \end{cases} \tag{19}$$

and each matrix is detailed in (20) shown at the bottom of the next page. The state variables of the system consist of the grid current, the phase angle of the CRF, and the integral of the current error, represented as $\widetilde{\mathbf{x}}_{\text{ss}} = \begin{bmatrix} \widetilde{\mathbf{i}}^m_{dq,o}{}^T & \widetilde{\phi}_c & \widetilde{\boldsymbol{\xi}}^c_{dq,o}{}^T \end{bmatrix}^T$. The system inputs include the grid voltages, grid frequency, and current references, denoted by $\widetilde{\mathbf{v}}_{dq,g}$, $\widetilde{\omega}_g$, and $\widetilde{\mathbf{i}}_{dq,\text{ref}}$, respectively. The impact of each input on the state variables is modeled by $\mathbf{B}$ matrices.

The outputs from the system are the currents and the instantaneous frequency of the grid-connected converter, represented by

$\widetilde{\mathbf{y}}_{\text{ss}} = \left[\widetilde{\mathbf{i}}^{m}_{dq,o}{}^{T} \quad \widetilde{\omega}_c\right]^T$. The construction of the state-space model $\mathbf{A}_{\text{ss}}$ utilizes subsystem matrices as blocks to outline the model comprehensively. The first row of blocks in $\mathbf{A}_{\text{ss}}$ is derived from the linearization of (17), the second row from the linearization of (15), and the third row from the linearization of (18). The matrices that relate the inputs and outputs to the system state variables are structured as block matrices. An nth order identity matrix is denoted by $\mathbf{I}_{n\times n}$. In a stable system, the steady-state response, as described in (19), ensures that $\mathbf{i}^{c}_{dq,\text{ref}} = \mathbf{i}^{c}_{dq,o}$.

Moreover, the matrix $\mathbf{R}^{\phi}(\phi_c) = \frac{d\mathbf{R}(\phi_c)}{d\phi_c}$ demonstrates the impact of variations in ϕ_c, stemming from synchronization dynamics, on both other state variables and itself. This effect is similar to the influence of the dynamics of a PLL on a grid-following converter, as described in [8].

The linearization process around an operating point produces a small-signal model whose dynamics are sensitive to parameter variations. These include changes in control parameters, voltage amplitude, steady-state currents, converter impedance, and grid impedance associations. The model also incorporates simplifications of the LCL filter, while discretization and LPFs are excluded. The dynamics of such components become significant for control systems with higher gains and pass bands around or over the grid frequency.

The accuracy of time-domain simulations is limited to minor variations in current setpoints, voltage amplitude, and frequency. More complex scenarios require an extended model. For example, operation in grids with unbalanced lines would require sequence domain models, and interactions with nonlinear loads would require harmonic state-space techniques [27].

The next section presents the stability analysis and control design. In addition, design considerations necessary for maintaining the stability of the converter throughout its operational range are discussed. Section V validates the linear model against an HIL implementation using time simulations.

IV. Stability and Design of the q-Axis Self-Synchronizing Current Control

The system formed by the grid-connected converter and the self-synchronizing current control results in a multiple-input multiple-output (MIMO) system whose eigenvalues vary as functions of its parameters. The root locus analysis for single-input single-output systems shows how eigenvalues trace paths from open-loop poles to open-loop zeros asymptotically. The behavior of the eigenvalues in MIMO systems is somewhat similar. This system has five eigenvalues allocated along trajectories from an open-loop pole to an open-loop zero of each feedback. In such a MIMO system, with more than one feedback, the graphical approach used in this article involves fixing one feedback and varying the others. The gain is chosen to ensure the eigenvalues are strategically positioned along these trajectories, assuring the system dynamic response meets the desired criteria. Table I presents the parameters of the three-phase grid-connected converter considered for the design through (19) and referred to Fig. 2(a).

TABLE I
Three-Phase Grid-Connected Converter Parameters

R_{ci} [Ω]	L_{ci} [μH]	R_{co} [Ω]	L_{co} [μH]	C_c [μF]	R_d [Ω]	V_{rms} [V]	V_0 [V]
0.01	625	0.01	625	30	1	220	180
Ω_0 [rad/s]	Ω_{lpf} [rad/s]	f_{sw} [kHz]	f_s [kHz]	T_s [μs]	S_n [kVA]	P_n [kW]	V_{dc} [V]
377	6283	20	20	50	24	20	500

First, the time constants T_D and T_Q are chosen as 0.02 s and 0.025 s, resulting in open-loop poles of the controller in 50 and 40 rad/s, respectively. After closing all the feedback with chosen gains, these open-loop poles result in dominant eigenvalues. The proportional gains are initially set to zero during the root locus analysis. The aim is to obtain critical damping of eigenvalues to avoid overshoots during transient responses.

Fig. 3 shows the trajectory of the eigenvalues as K_D changes; K_Q and K_{AQ} are set to zero. The right-hand sidebar indicates the variation of K_D, which is the gain of the d-axis current. As K_D increases, the open-loop poles from $\frac{R_{\text{eq}}}{L_{\text{eq}}} \pm j\Omega_0$ move to the position of critical damping, while one of the closed-loop poles decreases its real part. This last eigenvalue is the exceeding open-loop zero that goes indefinitely to the left in the direction of the real axis.

Fig. 4 shows the root locus analysis for the variations in K_Q, depicted in the right-hand sidebar. K_D is set to 2.0 and K_{AQ} is zero. K_Q is the proportional gain of the q-axis self-synchronizing current loop. As K_Q increases, the imaginary part increases more than the real part, and some eigenvalues become badly damped. The $K_Q = 1.5$ value is set, and the system is stable.

$$\mathbf{A}_{\text{ss}} = \begin{bmatrix} \mathbf{A}_{\text{ss},11} & \mathbf{A}_{\text{ss},12} & \mathbf{A}_{\text{ss},13} \\ -K_Q\mathbf{s}_2\mathbf{R}(\overline{\phi}_c) & -K_Q\mathbf{s}_2\mathbf{R}^{\phi}(\overline{\phi}_c)\overline{\mathbf{i}}^{m}_{dq,o} & \frac{K_Q}{T_Q}\mathbf{s}_2 \\ -\mathbf{R}(\overline{\phi}_c) & -\mathbf{R}^{\phi}(\overline{\phi}_c)\overline{\mathbf{i}}^{m}_{dq,o} & \mathbf{0}_{2\times 2} \end{bmatrix}, \mathbf{B}_{\text{ss,vg}} = \begin{bmatrix} -\frac{1}{L_{\text{eq}}}\mathbf{I}_{2\times 2} \\ \mathbf{0}_{2\times 2} \\ \mathbf{0}_{2\times 2} \end{bmatrix}, \mathbf{B}_{\text{ss},\omega g} = \begin{bmatrix} \mathbf{0}_{2\times 1} \\ -1 \\ \mathbf{0}_{2\times 1} \end{bmatrix}, \mathbf{B}_{\text{ss,ref}} = \begin{bmatrix} \frac{1}{L_{\text{eq}}}\mathbf{K}_C \\ K_Q\mathbf{s}_2 \\ \mathbf{I}^T_{2\times 2} \end{bmatrix}$$

$$\mathbf{C}_{\text{ss}} = \begin{bmatrix} \mathbf{I}_{2\times 2} & \mathbf{0}_{2\times 1} & \mathbf{0}_{2\times 2} \\ -K_Q\mathbf{s}_2\mathbf{R}(\overline{\phi}_c) & -K_Q\mathbf{s}_2\mathbf{R}^{\phi}(\overline{\phi}_c)\overline{\mathbf{i}}^{m}_{dq,o} & \frac{K_Q}{T_Q}\mathbf{s}_2 \end{bmatrix}, \mathbf{A}_{\text{ss},11} = -\frac{R_{\text{eq}}}{L_{\text{eq}}}\mathbf{I}_{2\times 2} - \frac{1}{L_{\text{eq}}}\mathbf{R}(-\overline{\phi}_c)\mathbf{K}_C\mathbf{R}(\overline{\phi}_c) - \mathbf{J}\Omega_0$$

$$\mathbf{A}_{\text{ss},12} = \frac{1}{L_{\text{eq}}}\left(\mathbf{J}\overline{\mathbf{v}}^{m}_{dq,i} - \mathbf{R}(-\overline{\phi}_c)\mathbf{K}_C\mathbf{R}^{\phi}(\overline{\phi}_c)\overline{\mathbf{i}}^{m}_{dq,o}\right), \mathbf{A}_{\text{ss},13} = \frac{K_D}{T_D L_{\text{eq}}}\mathbf{R}(-\overline{\phi}_c)\mathbf{S}_{11}, \mathbf{K}_C = \begin{bmatrix} K_D & 0 \\ 0 & K_{AQ} \end{bmatrix}, \mathbf{J} = \begin{bmatrix} 0 & -1 \\ 1 & 0 \end{bmatrix}, \mathbf{S}_{11} = \begin{bmatrix} 1 & 0 \\ 0 & 0 \end{bmatrix}. \tag{20}$$

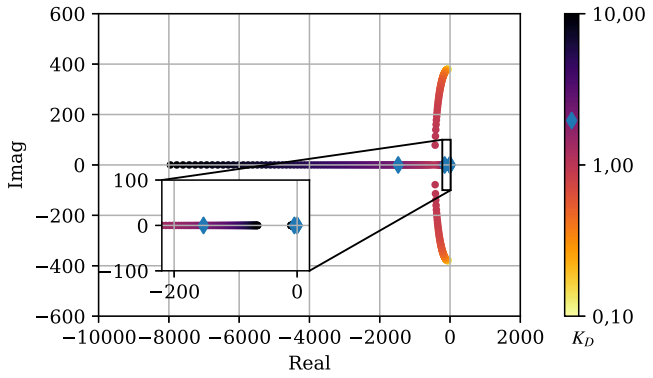

Fig. 3. Root locus analysis verifies the variation of the feedback gain, K_D. The loop of synchronization and q-axis current control are open, with $K_Q = 0$ and $K_{AQ} = 0$.

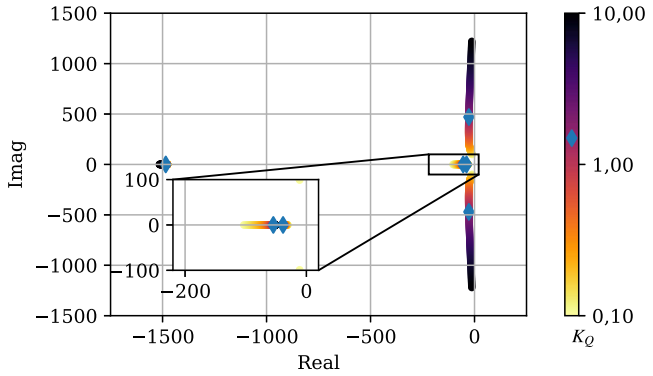

Fig. 4. Root locus analysis is performed to verify the impact of feedback gain K_Q of the synchronization loop and the quadrature current control. The direct current loop is closed with $K_D = 1$, while the quadrature voltage loop is still open, with $K_{AQ} = 0$.

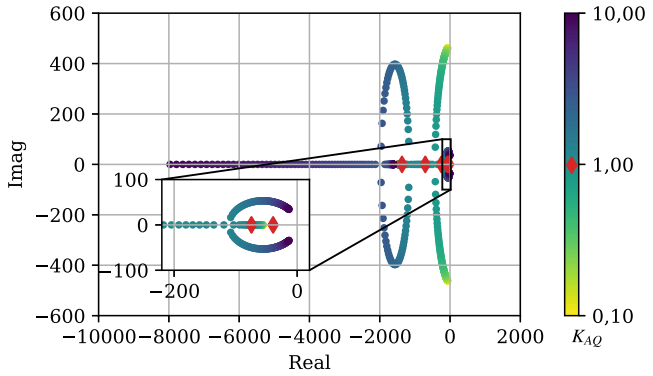

Fig. 5. Root locus analysis is performed to verify the impact of K_{AQ} with $K_D = 1$ and $K_Q = 1.77$: the damping of eigenvalues increases as K_{AQ} increases.

Fig. 5 illustrates the root locus analysis for varying K_{AQ} values, as indicated on the right-hand sidebar while maintaining $K_D = 2$ and $K_Q = 1.5$. This feedback adds the q-axis voltage that counteracts errors in the q-axis current. It effectively mitigates the oscillations in this current used for frequency calculation, leading to eigenvalues with enhanced damping. Setting $K_{AQ} = 1.0$ achieves overdamping, preventing overshoot during the system transient response. As this transient fades, the error in the q-axis current diminishes to zero due to the integrator used in frequency calculation. Incorporating the proportional gain K_{AQ} introduces additional damping into the system, and it does not impact the steady-state behavior of this control. The increased damping is analogous to adding a virtual resistance [12], [28]. Section V-F analyzes this impact in detail.

TABLE II
DESIGNED CONTROL PARAMETERS

K_D $\left[\frac{\text{V}}{\text{A}}\right]$	T_D $\left[\frac{\text{V}}{\text{sA}}\right]$	K_Q $\left[\frac{\text{rad}}{\text{sA}}\right]$	T_Q $\left[\frac{\text{rad}}{\text{s}^2\text{A}}\right]$	K_{AQ} $\left[\frac{\text{V}}{\text{A}}\right]$
2.0	0.02	1.5	0.025	1.0

Fig. 5 shows, finally, markers that indicate the eigenvalues obtained with control parameters from Table II: $\lambda_1 = -42.61$, $\lambda_2 = -63.19$, $\lambda_3 = -276.8$, $\lambda_4 = -690.74$, and $\lambda_5 = -1342.65$.

In this design methodology, T_D and T_Q define open-loop zeros that are an approximated target to the dominant closed-loop dynamics of the control. In this regard, a change in any parameter does not modify these zeros, but it affects the location and trajectories of the dominant eigenvalues in the complex plane.

In $\mathbf{A}_{\text{ss}}$, the parameters $\overline{\mathbf{v}}^m_{dq,i}$, L_{eq} and K_Q forms the blocks $\mathbf{A}_{\text{ss},12}$ and $-K_Q \mathbf{s}_2 \mathbf{R}(\overline{\phi}_c)$ that represent the q-axis self-synchronizing feedback loop. In this loop, the q-axis current is more susceptible to changes of ϕ_c as the voltages are higher and inductance is smaller. In such situations, the synchronization feedback is stronger, and a smaller K_Q gain is needed. Conversely, a large K_Q is needed for lower voltages and large inductance. Changes in the synchronization dynamics require adjustments of the damping K_{AQ}.

The d-axis current control and the damping effect of K_{AQ} are susceptible to changes in impedance parameters. In resistive-inductive lines, the combination of K_D, K_{AQ}, R_{eq}, and L_{eq} results in different time constants for the d- and q-axis currents. For higher R_{eq} and lower L_{eq}, lower values of K_D and K_{AQ} are needed, and the reciprocal is true. $\mathbf{A}_{\text{ss},11}$ in (20) is a diagonal block dependent on these terms. Considering the structure of $\mathbf{A}_{\text{ss}}$, increasing K_D and K_{AQ} makes the trace of $\mathbf{A}_{\text{ss}}$ more negative, resulting in lower accommodation times and better stability. However, higher gains may trigger oscillations due to dynamics not included in the small-signal model. An overdamped design, as presented in this section, is recommended to mitigate stability issues arising from variations in operating conditions.

The following section shows real-time simulations that include a start-up process, validation of the linear model, and operation in grids with nonideal voltages.

V. VERIFICATION OF THE q-AXIS SELF-SYNCHRONIZING CURRENT CONTROL

Fig. 6 shows the real-time simulation test bench used. It consists of a Typhoon HIL 604 with a multiple microcontroller interface board, the μgrid DSP interface from Typhoon. The proposed self-synchronizing current control is implemented on a Texas TMS320F28335 control card and validated on the test bench. The converter depicted in Fig. 2(a) is virtualized in

Fig. 6. Typhoon HIL-604, μgrid DSP interface board, and TMS320F28335 microcontroller used in the HIL verification.

the Typhoon HIL characterizing the so-called HIL real-time simulation [29]. The parameters for the controller and converter are listed in Tables I and II.

This section includes a start-up process in Section V-A. Sections V-B–V-D investigate the response of the system to voltage sags, harmonic disturbances, and different grid impedances under the proposed design. Section V-E validates the linear model, and finally, Section V-F analyzes changes in power flow and the changes in stability provided by adding K_{AQ}.

A. Start-Up of the Self-Synchronizing Control

The proposed self-synchronizing current control must have the SRF correctly set to initialize adequately in practical situations. High current overshoots may occur if a significantly different phase angle exists between SRF and CRF. To avoid it, starting the SRF with phase and frequency close to the CRF operating point is important, so this section presents a start-up procedure.

When the pulsewidth modulation (PWM) switching is disabled, the capacitor dominates the LCL impedance observed by the grid. In this scenario, if $\mathbf{v}^m_{dq,g}$ includes only the d-axis component (i.e., q-axis is null), the LCL current presents the q-axis component significantly larger than the d-axis component

$$\mathbf{i}^m_{dq,o} \approx \begin{bmatrix} 0 \\ -\Omega_0 C_c \overline{v}^m_{d,g} \end{bmatrix}. \tag{21}$$

The q-axis current of (21) is proportional to the grid voltage magnitude. This current measurement allows the voltage estimation when the grid-connected converter is not switching. A current-based PLL is then employed at the start-up, so the converter frequency is given by

$$\omega_c = \Omega_0 + K_{id} i^c_{d,o}. \tag{22}$$

However, this estimation requires the LCL filter to remain continuously connected to the grid, while only the switches and the internal inductor may be disconnected. The CRF angle θ_c during the start-up is a result of the integration of converter frequency, as shown in (2). The steps to change the converter frequency and current setpoints from the start-up to the self-synchronizing current control are listed next.

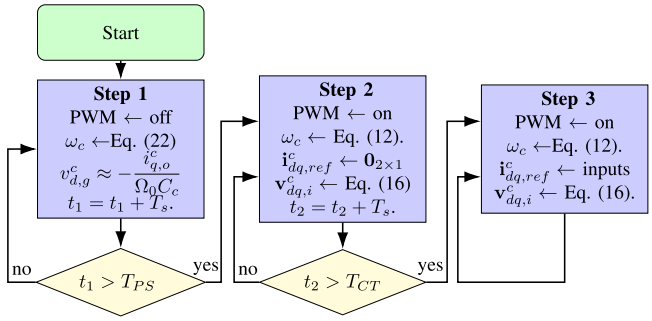

Fig. 7. Flowchart for the start-up procedure. Steps 1 and 2 operate for limited time, and step 3 operates indefinitely.

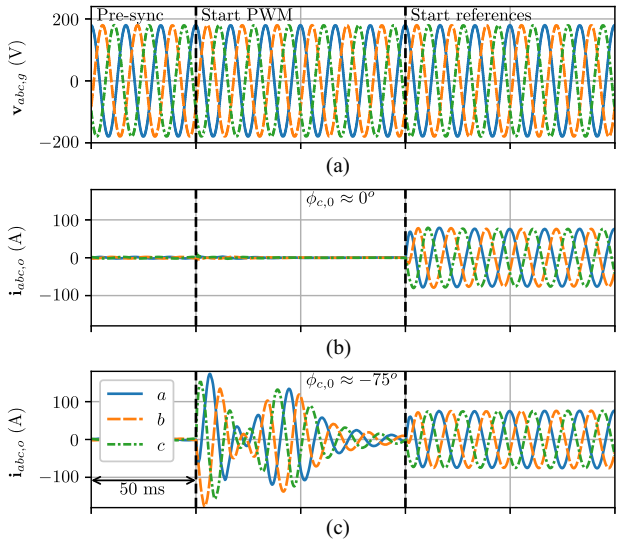

Fig. 8. Initialization of the grid-connected converter. (a) Three-phase voltages of the grid. (b) Three-phase currents of the grid-connected converter with an angle difference of 0° at the start-up. (c) Three-phase currents of the grid-connected converter with an angle difference of 75° at the start-up.

Step 1: First, the initial synchronization through the current-based PLL occurs. Equation (22) defines the CRF frequency. After a settling time for the presynchronization step (T_{PS}), initiate Step 2.

Step 2: Next, the control is initialized with a zero-current setpoint to prevent abrupt changes in the output currents due to deviations in grid voltages from nominal values. After a settling time for the initial current transients (T_{CT}), initiate Step 3. The PWM starts, and now (12) defines the CRF frequency.

Step 3: Finally, new setpoints can be placed once the converter reaches the steady-state operation. The converter frequency is obtained by (12) during the rest of the operation.

Fig. 7 shows a flowchart for the start-up procedure. The timers t_1 and t_2 count the waiting times T_{PS} and T_{CT}, respectively. T_{PS} and T_{CT} are fixed in 0.1 s for this process, but they must be determined based on the dynamic response and settling time of the controlled system.

Figs. 8 and 9 show HIL results for the start-up procedure. The "Pre-sync" interval corresponds to Step 1. This step closely aligns the CRF with the grid voltage vector using the current

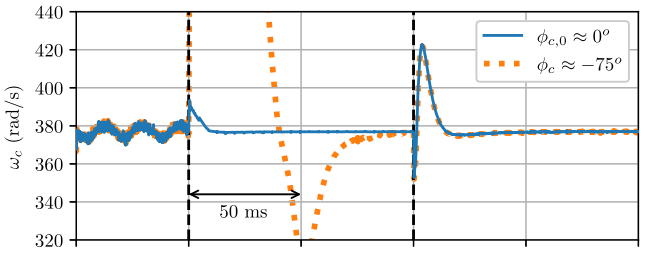

Fig. 9. Frequency of the grid-connected converter during the initialization of the grid-connected converter: frequency and current transient diminished after proper initialization.

flowing through the LCL filter. The "Start PWM" interval corresponds to Step 2. The synchronization is maintained when the converter is not actively operating, enabling the converter to be initialized at any time with minimal initial transient, which occurs in "Start references" interval and corresponds to Step 3.

Fig. 8(a) and (b) shows the grid voltages and the converter currents when the self-synchronizing current control starts with a slight angle difference from the MRF, respectively. As a result, the currents present minimal disturbance, gradually reducing to zero within 0.1 s in the "Start PWM" interval. The converter then starts to track a current reference of approximately 76.4 A. The currents in Fig. 8(b) are synchronized with the voltages in Fig. 8(a).

Fig. 8(c) shows the converter currents when the start-up procedure is not used and a phase angle difference of about -75° exists. The significant angle difference results in a transient with peak values exceeding the setpoint of 74.6 A by more than 100%. In such conditions, the control still achieves synchronization to the grid voltages after the end of the current transient. However, the system may become unstable for more significant starting angle differences.

Fig. 9 shows the converter frequency during initialization. When the control is initialized correctly (initial phase difference of approximately 0°), the initial transient of the converter frequency is small. When the control is not initialized correctly (initial phase of -75°), the required control effort for the synchronization increases, resulting in transients in ω_c with variations exceeding 62.8 rad/s.

B. Operation During Voltage Sags

Fig. 10(a) and (b) shows the grid-connected converter three-phase voltage and current for a symmetrical 50% voltage sag. From (19), $\mathbf{v}_{dq,i}^{m}$ is included in $\mathbf{A}_{\text{ss},12}$, which implies that the grid voltage also influences the feedback of the synchronization loop represented by ϕ_c. As the voltage sag occurs, the current increases. However, after the voltage is set at 50% of the nominal value, the current tracks the previous setpoint after 0.05 s. When the voltage is restored, the current decreases. The same occurs after voltage restoration. The zoomed waveforms show that the current keeps synchronizing with the voltage during the voltage sag. The result shows that the self-synchronizing current control can provide inherent low-voltage ride-through capability by limiting the steady-state currents with zero error without additional changes in control. This approach is fundamentally different from conventional PSCs.

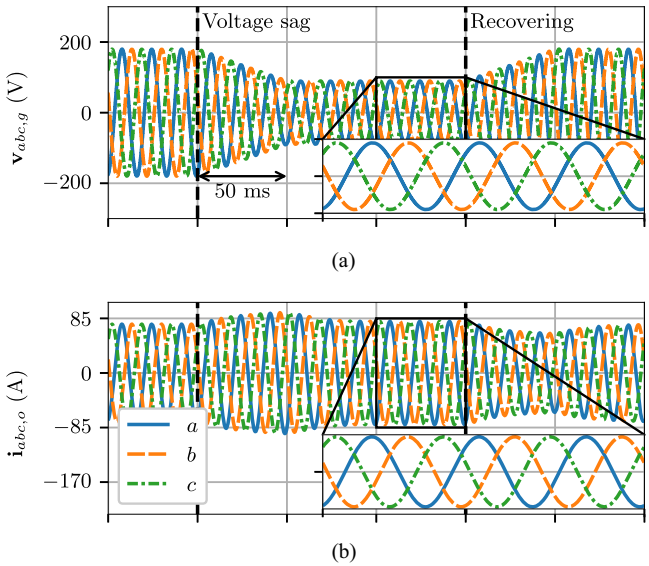

Fig. 10. 50% three-phase voltage sag occurrence during the operation of the grid-connected converter. (a) Thee-phase phase voltages of the grid. (b) Three-phase currents of the grid-connected converter.

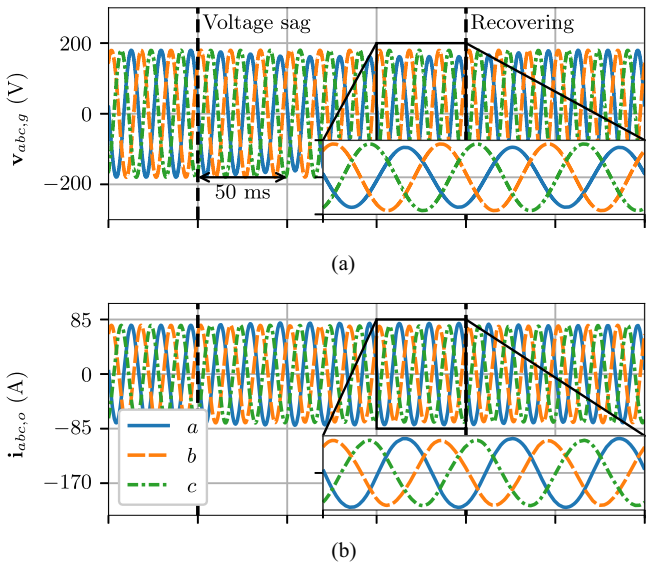

Fig. 11. 10% single-phase voltage sag occurrence during the operation of the grid-connected converter. (a) Thee-phase phase voltages of the grid. (b) Three-phase currents of the grid-connected converter.

Fig. 11(a) and (b) shows the voltages and currents during the occurrence of a 10% single phase voltage sag in phase a. No sags occur in phase b and c voltages. Note there are minor changes in the current amplitude: phase a current increases by 3 A, while phases b and c decrease by 1.5 A. Even though a negative sequence current appears, the detailed waveforms in Fig. 11(a) and (b) show that the currents are synchronized to the voltages. The self-synchronizing current control, as designed, regulates the positive sequence properly, but additional

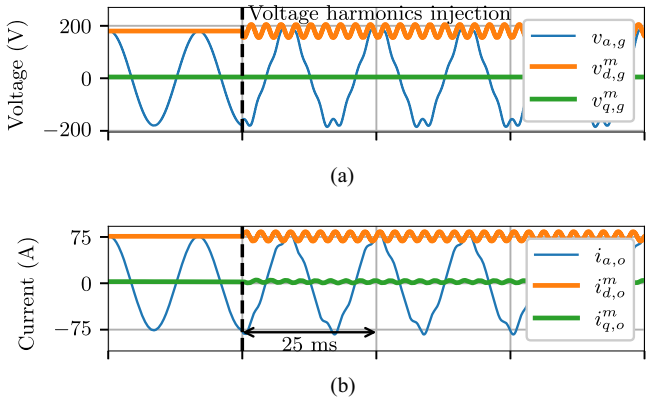

Fig. 12. Operation under distorted grid voltage with 10-% TDH. (a) Phase a and dq-frame grid voltages. (b) Phase a and dq-frame converter currents.

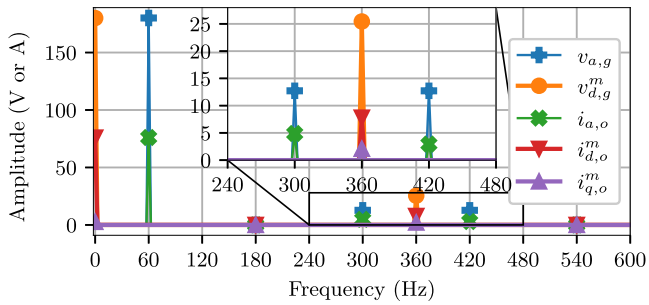

Fig. 13. FFT analysis of phase a and dq-frame grid voltages and converter currents.

controllers are required if the negative sequence current should be mitigated, which are discussed in the literature. One option is introducing resonant controllers to counterbalance the disturbances in dq-frame currents [30]. Another option is a dual SRF, one establishing control for the positive sequence and the other for the negative sequence [30]. The design of additional controllers is out of the scope of this work.

C. Operation in Distorted Grids

Fig. 12(a) and (b) presents the operation under distorted grid voltage with a total harmonic distortion (THD) of 10%. Each phase voltage includes fifth- (negative sequence) and seventh-order harmonics (positive sequence), both with a 12.73-V amplitude. Fig. 12(a) shows the phase a and the dq-frame grid voltages. The dc component of the d- and q-axis grid voltages is 180 V and 0 V, respectively, and a 360-Hz sinusoidal component is result of the harmonic distortion in the dq-frame. Fig. 12(b) shows the phase a and the dq-frame converter currents. The phase a current includes the distortion of fifth- and seventh-order harmonics distortion, while the dq-frame currents have a dc component and a 360-Hz sinusoidal component.

Fig. 13 shows a fast Fourier transformation (FFT) analysis of phase a and dq-frame grid voltages and converter currents. Converter current includes fifth- and seventh-order harmonics of 4.88-A and 2.94-A amplitude, respectively. Note that the change from the abc-frame to the dq-frame is equivalent to a frequency

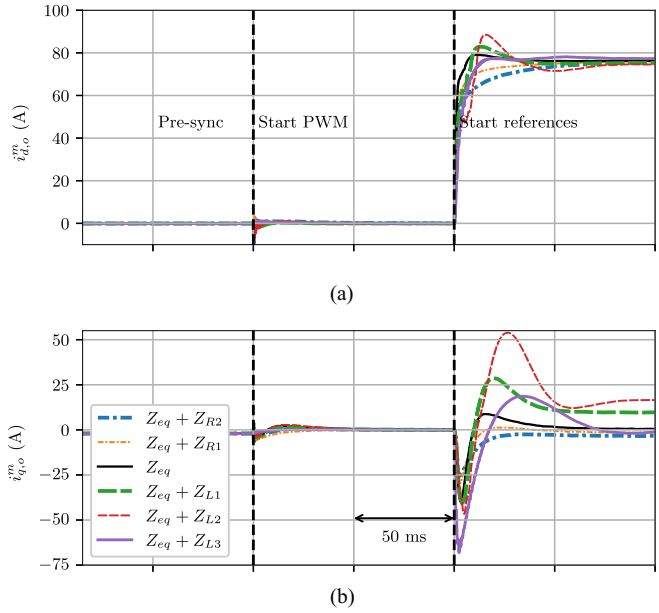

Fig. 14. Grid-connected converter start-up when parameter variation is applied. (a) Converter currents in the d-axis. (b) Converter current in the q-axis.

shift of the harmonics components, e.g., the fundamental component of the abc-frame is equivalent to the dc component (0 Hz) of the dq-frame. However, the fifth- and seventh-order harmonics of the abc-frame are both grouped to the 360-Hz component of the dq-frame due to their negative and positive sequence terms, respectively. The amplitude of d- and q-axis currents is 7.79 A and 2.08 A, respectively, and the current THD is 7.5%.

The self-synchronizing control, as designed, can maintain synchronization when voltage harmonics exist, but distorted currents result from the distorted voltage. One may conclude that the self-synchronizing control cannot attenuate the grid voltage harmonics to the currents. However, additional controllers can be included alongside further gain adjustment, so the effects of the distorted grid are mitigated properly. This is already fairly discussed for grid-following converters in distorted voltage grids [31], [32]. Thus, a further discussion on the additional controllers is out of the scope of this work.

D. Effects of Grid Impedance and Parameter Variation

Fig. 14 shows the d-axis and q-axis currents during the startup process described in Section V-A when the grid-connected converter interfaces a pure resistive line ($Z_{R2} = 0.5\,\Omega$, $Z_{R1} = 0.25\,\Omega$) or a pure inductive line ($Z_{L1} = j0.235\,\Omega$, $Z_{L2} = j0.471\,\Omega$ and $Z_{L3} = j1.414\,\Omega$). Fig. 14(a) and (b) also includes the case for only Z_{eq} for comparison.

As a d-axis reference current of 76.4 A is set, a 11.19°-phase shift appears both in the CRF and in the currents due to the effect of the equivalent impedance, $Z_{\text{eq}} = R_{\text{eq}} + j\Omega_0 L_{\text{eq}} = 0.02\,\Omega + j0.471\,\Omega$. This would result in an approximately 13 A q-axis current, and the resulting $\cos(\phi_c)$ is 0.981, which points out a reduced power factor. Equation (11), however, compensates for this deviation. As a result, the q-axis current is approximately

zero, as shown by the curve Z_{eq} in Fig. 14(b), and the power factor is 0.999.

The grid impedance is usually modeled as a resistive–inductive line. Its direct effect on the grid-connected converter is to yield an output filter with a distinct impedance characteristic. Usually, it consists of additional resistive and inductive components. From the converter's point of view, this effect is similar to the impact of parameter changes or mismatches from the design stage. Fig. 14(a) shows that the steady state of the d-axis current is unaffected by parameter deviations or series association with line impedance. The power factor for Z_{eq}-only case is approximately 0.999. Fig. 14(b) shows that that steady state q-axis currents are approximately 9.5 A and 16.5 A when associated with Z_{L1} and Z_{L2}. The resultant current phase has cosines of 0.992 and 0.977, respectively. In contrast, resistive lines Z_{R2} and Z_{R1} do not absorb reactive power and, therefore, affect the power factor negligibly.

Note that the case $Z_{L3} = j1.414\,\Omega$ represents a weak grid with a short circuit ratio of 1.7. Due to the significant influence of the grid impedance, a redesign of the controller resulted in new proportional gains $K_D = 8$, $K_Q = 5$, and $K_{AQ} = 8$. To achieve the same step response as the previous data, V_{dc} was also increased to 700 V. The results demonstrate a dynamic similar to the previous cases. Analysis with large-signal models could provide more insight into the self-synchronizing control in weak grids. Nevertheless, the results show that, with proper design, the self-synchronizing control can operate effectively in weak grids.

As a partial conclusion, the grid-connected converter maintains its stability, although the dynamics are affected by the parameter errors or the association with an inductive or resistive line. An equivalent increased resistance enhances the converter damping, while an increased inductance decreases it. Therefore, designing a grid-connected converter that accounts for an estimated grid impedance offers an advantage when using self-synchronizing control, as it is more reliable in weak grids than PLL-based control, which is prone to failure. Also, the compensation of reactive power presents errors when not accounting for the line impedance, decreasing the power factor. Including an accurate output impedance may overcome this issue, but it is not an obvious task due to the uncertainties of the grid impedance for specific applications.

E. Comparison of Linear and Real-Time Simulations

This section presents a simulation applying the linearized model in Section III-D using the Python Control Systems Library [33]. The linear model is compared to real-time simulations in the Typhoon HIL. Comparisons are made to assess the accuracy of the linearized model. The converter and control parameters are in Tables I and II. Specifically, the system response to a step change in the magnitude and frequency of the voltage is used as a benchmark. The following sections present the results and analysis of this comparison.

1) Step Change in Voltage Magnitude: Fig. 15 illustrates the dq-frame currents in the MRF and ω_c, reacting to a change in the grid-voltage magnitude. Initially, the MRF is in sync with the voltage vector at the coupling point, with the d-axis component representing the current vector magnitude. When a 5-V step is applied to the d-axis grid voltage, it triggers a transient response, causing the d-axis current to decrease to about 74 A. This event also leads to oscillations in the q-axis currents due to the dq-frame coupling. Nonetheless, the current stabilizes to its original set point within 50 ms. The converter frequency exhibits a similar disturbance pattern, returning to its initial value following the transient.

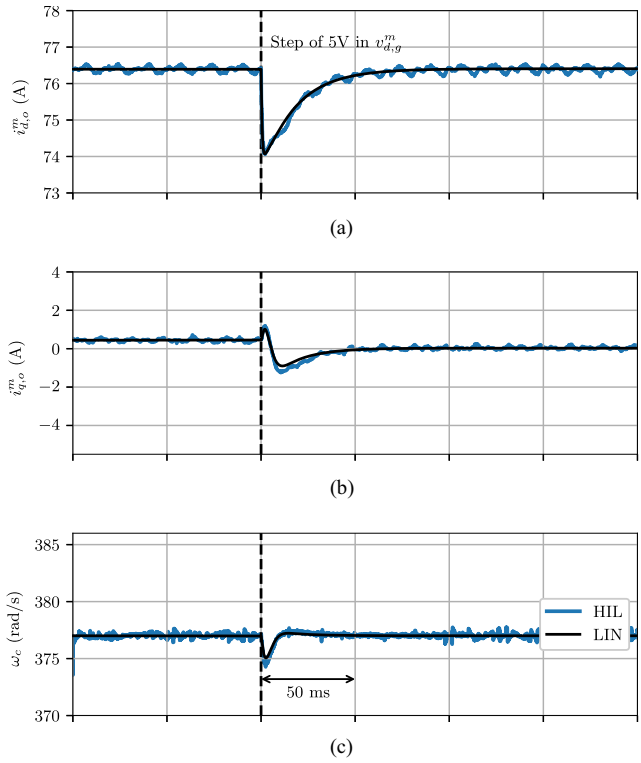

Fig. 15. Linearized model and HIL test results for a step of 5 V in the magnitude of the grid voltage. (a) Converter currents in the d-axis. (b) Converter currents in the q-axis. (c) Converter frequency.

2) Step Change in Frequency: Fig. 16 presents the MRF currents and the grid-connected converter angular frequency, initially 377 rad/s (60 Hz), as they respond to a 6.28 rad/s (1 Hz) step change in the grid voltage. The transient behavior in the currents stems from a frequency mismatch between the grid voltage and the CRF. This discrepancy results in a phase angle disturbance, prompting the control system to adjust its frequency to match the grid frequency.

The self-synchronizing current control demonstrates its ability to maintain synchronization despite frequency changes. The currents gradually return to their steady-state values as the control system adjusts to the new frequency. Despite the inherent nonlinearity of the system, the linearized model effectively captures the dynamics of the currents and frequency. This modeling accuracy facilitates the system design, presenting appropriate and desired responses under various operational conditions.

F. Effect of Power Flow and Additional Damping on the Stability

Changing the power flow of the grid-connected converter through a line with no impedance allows us to observe the sensibility of the q-axis self-synchronizing current control to

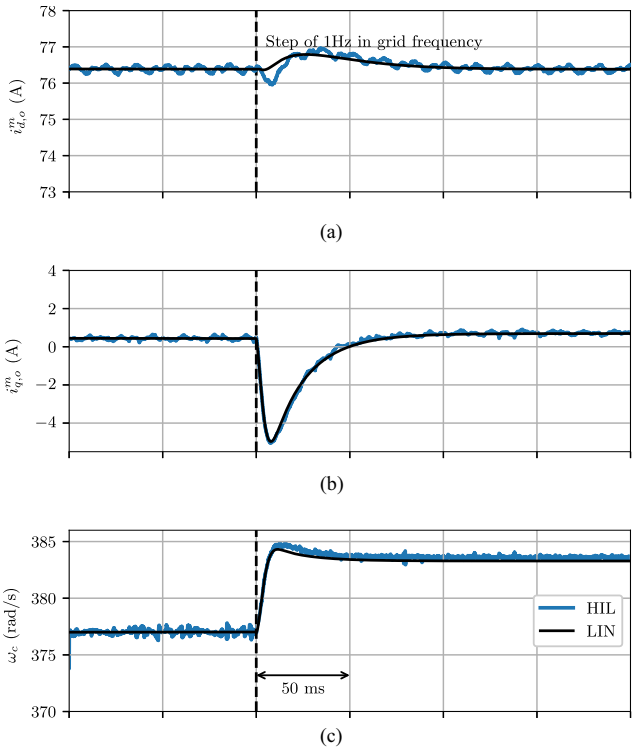

Fig. 16. Linearized model and HIL test results for a step of 1 Hz in the grid voltage frequency. (a) Converter currents in the d-axis. (b) Converter currents in the q-axis. (c) Converter frequency.

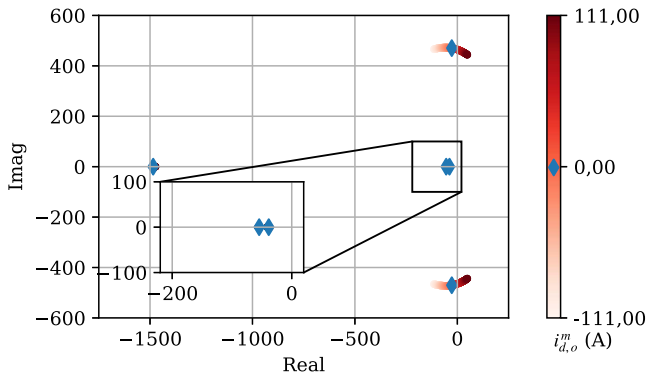

Fig. 17. Impact of the variation of the injected power from −30 to 30 kW on the stability of the converter. The direct current loop is closed with $K_D = 2$, $K_Q = 1.5$ when the quadrature voltage gain K_{AQ} is zero.

such changes. The parameters used are in Tables I and II, but the strategy of introducing additional damping is not applied in Fig. 17 by setting $K_{AQ} = 0$. When current increases, there is a loss of damping to a system that presents eigenvalues poorly damped. The damping diminishes as the injected current increases, and the system becomes unstable above specific current values.

The element at position (2,2) in the matrix $\mathbf{A}_{ss}$ of (19) contributes to the instability. This element is equal to $K_Q \tilde{\mathbf{i}}^c_{d,o}$. It means that positive values of the d-axis current affect the trace of $\mathbf{A}_{ss}$, making it more positive and potentially moving some eigenvalues to the right semiplane. In other words, the more

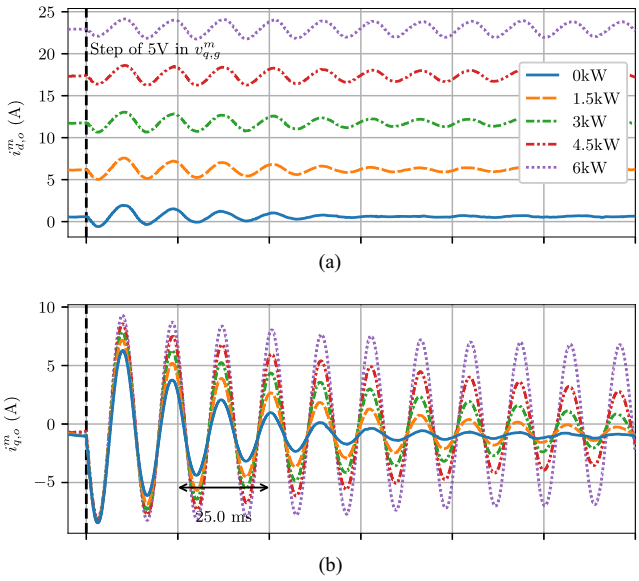

Fig. 18. Synchronization dynamics to a step of 5 V in $v^m_{q,g}$ when active power flows (max. 6 kW) and $K_D = 2$, $K_Q = 1.5$, and $K_{AQ} = 0$. (a) Converter currents in the d-axis. (b) Converter currents in the q-axis.

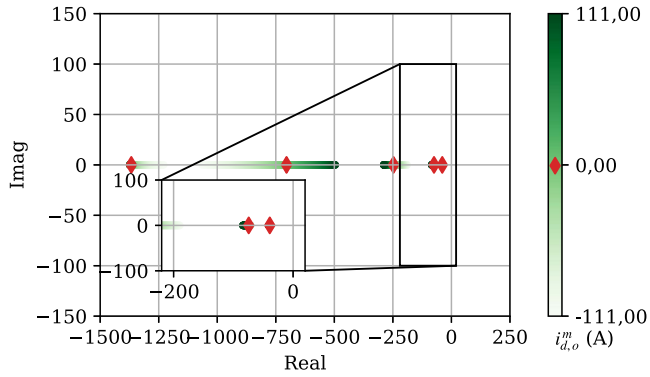

Fig. 19. Eigenvalues under variations of the active power from −30 to 30 kW on the synchronization dynamics when the gain K_{AQ} is 1.

active power the grid-connected converter injects, the closer it becomes to instability.

This phenomenon is observable in real-time HIL tests by observing the grid-connected converter response to minor changes in the grid voltage angle. In Fig. 18, a 5-V step change in the q-axis voltage of the grid, equivalent to about a 1.59° shift in the phase angle of the voltage, disrupts the operation of the converter. This results in a similar reduction of the damping, with oscillations in the currents persisting for over 150 ms when the $i^m_{d,o}$ current is around 23 A, indicating the system is prone to instability.

An essential difference between this self-synchronizing control and controls employing a PLL is that the voltage magnitude is approximately constant during regular operation. Conversely, as the current varies, the synchronization loop dynamics change, which affects the self-synchronizing current control system. Increasing the damping of the phase angle is necessary to mitigate these effects and ensure system stability.

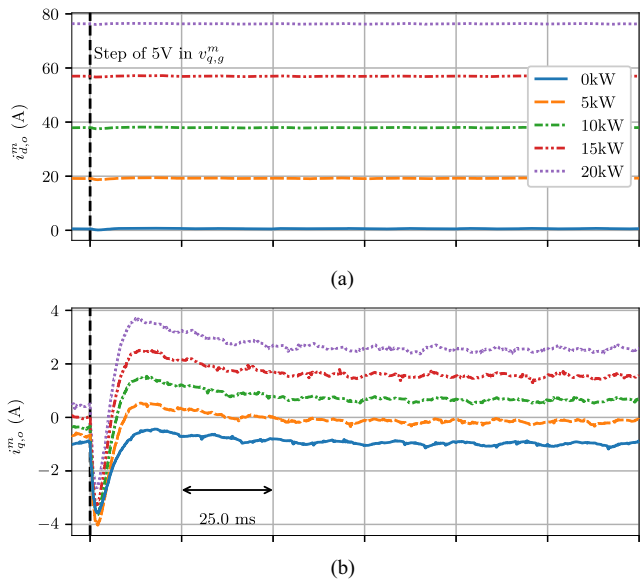

Fig. 20. Synchronization dynamics to a step of 5 V in $v^m_{q,g}$ when active power flows (max. 20 kW) and $K_D = 2$, $K_Q = 1.5$, and $K_{AQ} = 1$. (a) Converter currents in the d-axis. (b) Converter currents in the q-axis.

Fig. 19 shows the root locus analysis for $K_{AQ} = 1$, as designed in Section IV. The markers in Fig. 19 are in the same position as those in Fig. 5. They show the eigenvalues when the current is zero. As the current varies, the eigenvalues move, but the system damping is not reduced, which ensures stability throughout its full operating range. Notably, the dominant eigenvalue remains unchanged despite the large variation in the current. Therefore, the proposed design yields eigenvalues that maintain consistent damping.

Fig. 20 shows the response of the system with $K_{AQ} = 1$ to the 5-V step change in the q-axis grid voltage. The grid-connected converter shows well-damped transients, and larger d-axis currents do not significantly alter the response of the converter to changes in the phase angle of the grid voltage. The steady-state response shows larger values of the q-axis current when the d-axis current increases. This is a result of the phase angle shift in the grid voltage, which prompts the current of the grid-connected converter to track the change.

This section yields two key findings. First, the control of this grid-connected converter is sensible to the d-axis component of the current. Second, introducing a voltage component to damp oscillations in the q-axis current significantly enhances system stability.

VI. Conclusion

This article extends the characteristics of simultaneous regulation and synchronization found on grid-forming converters to a q-axis self-synchronizing control for current-controlled converters. The primary application of this approach is to provide a grid-connected converter that can solely depend on current measurements to synchronize with the grid while performing the current control actions. Such feature may allow the following:

1) the use of fewer sensors;
2) the replacement of PLL-based controllers in converters connected to weak grids;
3) the combination with a voltage controller [12], which can result in self-synchronizing grid-forming converters with intrinsic current limiting capability.

The self-synchronizing control maintains synchronization to symmetrical three-phase and single-phase voltage sags. However, to mitigate unbalanced currents due to asymmetrical faults, additional regulation strategies are needed. Resonant controllers also may be required to prevent current distortion when operating in grids with highly distorted voltages.

The modeling, analysis, and results of HIL simulation showed the feasibility of the proposed method. This approach introduced an additional feedback gain K_{AQ} to the self-synchronizing current control. This results in a q-axis voltage component that damps phase swings in the respective synchronization loop. The introduction of this gain results in extended and systematic stability, as shown by the eigenvalues analysis and the HIL test results. Further analysis detailed the impact of power flow on synchronization dynamics, showing that when the d-axis current increased, the damping provided by K_{AQ} ensured control stability across a significantly wider operating range. A linearized state-space model was developed, closely aligning with real-time HIL simulations. This model facilitated in-depth analysis of the grid-connected converter control system and supported a comprehensive design framework.

Furthermore, a compensation method for the LCL filter reactive power avoids reduced power factor during operation. This article also presents a start-up method that is absent in the existing literature. This method mitigates overcurrents at start-up by using the current flowing through the LCL filter capacitor to determine the grid voltage's amplitude and phase. In this approach, a current-based PLL operates only at start-up and synchronizes the CRF with the grid before starting operation.

Future will focus on the interactions among grid-connected converters using this control and the impact of its application on the grid. Also, analysis of large-signal models can provide deeper insights into the nonlinearities and limitations of the self-synchronizing loop. Further research using adaptive techniques could address the loss of damping caused by changes in the grid impedance. In addition, the design of additional controllers to mitigate the effects of voltage harmonics and unbalanced voltages in the converter current needs to be considered. Finally, other control actions of the grid-connected converter, such as ancillary services and islanding detection, must also be considered.

References

[1] J. Rocabert, A. Luna, F. Blaabjerg, and P. Rodríguez, "Control of power converters in ac microgrids," *IEEE Trans. Power Electron.*, vol. 27, no. 11, pp. 4734–4749, Nov. 2012.
[2] X. Wang, M. G. Taul, H. Wu, Y. Liao, F. Blaabjerg, and L. Harnefors, "Grid-synchronization stability of converter-based resources—An overview," *IEEE Open J. Ind. Appl.*, vol. 1, pp. 115–134, 2020.
[3] Y. Li, Y. Gu, and T. C. Green, "Revisiting grid-forming and grid-following inverters: A duality theory," *IEEE Trans. Power Syst.*, vol. 37, no. 6, pp. 4541–4554, Jun. 2022.
[4] V. Kaura and V. Blasko, "Operation of a phase locked loop system under distorted utility conditions," *IEEE Trans. Ind. Appl.*, vol. 33, no. 1, pp. 58–63, Jan. 1997.

[5] P. Rodríguez, R. Teodorescu, I. Candela, A. V. Timbus, M. Liserre, and F. Blaabjerg, "New positive-sequence voltage detector for grid synchronization of power converters under faulty grid conditions," in *Proc. 37th IEEE Power Electron. Specialists Conf.*, 2006, pp. 1–7.
[6] P. Rodríguez, J. Pou, J. Bergas, J. I. Candela, R. P. Burgos, and D. Boroyevich, "Decoupled double synchronous reference frame PLL for power converters control," *IEEE Trans. Power Electron.*, vol. 22, no. 2, pp. 584–592, Feb. 2007.
[7] M. Eskandari, A. V. Savkin, H. H. Alhelou, and F. Blaabjerg, "Explicit impedance modeling and shaping of grid-connected converters via an enhanced PLL for stabilizing the weak grid connection," *IEEE Access*, vol. 10, pp. 128874–128889, 2022.
[8] B. Wen, D. Boroyevich, P. Mattavelli, Z. Shen, and R. Burgos, "Influence of phase-locked loop on input admittance of three-phase voltage-source converters," in *Proc. 28th Annu. IEEE Appl. Power Electron. Conf. Expo.*, Mar. 2013, pp. 897–904.
[9] L. Harnefors, M. Hinkkanen, U. Riaz, F. M. M. Rahman, and L. Zhang, "Robust analytic design of power-synchronization control," *IEEE Trans. Ind. Electron.*, vol. 66, no. 8, pp. 5810–5819, Aug. 2019.
[10] N. Mohammed, H. Udawatte, W. Zhou, D. J. Hill, and B. Bahrani, "Grid-forming inverters: A comparative study of different control strategies in frequency and time domains," *IEEE Open J. Ind. Electron. Soc.*, vol. 5, pp. 185–214, Mar. 2024.
[11] L. Zhang, L. Harnefors, and H.-P. Nee, "Power-synchronization control of grid-connected voltage-source converters," *IEEE Trans. Power Syst.*, vol. 25, no. 2, pp. 809–820, Feb. 2010.
[12] L. Harnefors, J. Kukkola, M. Routimo, M. Hinkkanen, and X. Wang, "A universal controller for grid-connected voltage-source converters," *IEEE Trans. Emerg. Sel. Topics Power Electron.*, vol. 9, no. 5, pp. 5761–5770, May 2021.
[13] P. Wang et al., "Power self-synchronization control of grid-forming voltage-source converters against a wide range of short-circuit ratio," *IEEE Trans. Power Electron.*, vol. 38, no. 12, pp. 15419–15432, Dec. 2023.
[14] J. L. R. Amenedo, S. A. Gómez, J. Alonso-Martinez, and M. G. De Armas, "Grid-forming converters control based on the reactive power synchronization method for renewable power plants," *IEEE Access*, vol. 9, pp. 67989–68007, 2021.
[15] A. P. Asensio, S. A. Gomez, J. L. Rodriguez-Amenedo, and M. A. Cardiel-Álvarez, "Reactive power synchronization method for voltage-sourced converters," *IEEE Trans. Sustain. Energy*, vol. 10, no. 3, pp. 1430–1438, Mar. 2019.
[16] B. Liu, J. Liu, Z. Liu, T. Wu, and R. An, "An accurate power control scheme for droop-controlled grid-connected inverters," in *Proc. IEEE Appl. Power Electron. Conf. Expo.*, 2018, pp. 2374–2378.
[17] J. He and Y. W. Li, "An enhanced microgrid load demand sharing strategy," *IEEE Trans. Power Electron.*, vol. 27, no. 9, pp. 3984–3995, Sep. 2012.
[18] Q.-C. Zhong and G. C. Konstantopoulos, "Current-limiting droop control of grid-connected inverters," *IEEE Trans. Ind. Electron.*, vol. 64, no. 7, pp. 5963–5973, Jul. 2017.
[19] M. Alqatamin, J. Latham, Z. T. Smith, B. M. Grainger, and M. L. McIntyre, "Current control of a three-phase, grid-connected inverter in the presence of unknown grid parameters without a phase-locked loop," *IEEE Trans. Emerg. Sel. Topics Power Electron.*, vol. 9, no. 3, pp. 3127–3136, Jun. 2021.
[20] N. Pogaku, M. Prodanovic, and T. C. Green, "Modeling, analysis and testing of autonomous operation of an inverter-based microgrid," *IEEE Trans. Power Electron.*, vol. 22, no. 2, pp. 613–625, Feb. 2007.
[21] V. Mariani, F. Vasca, J. C. Vásquez, and J. M. Guerrero, "Model order reductions for stability analysis of islanded microgrids with droop control," *IEEE Trans. Ind. Electron.*, vol. 62, no. 7, pp. 4344–4354, Jul. 2015.
[22] R. Majumder, B. Chaudhuri, A. Ghosh, R. Majumder, G. Ledwich, and F. Zare, "Improvement of stability and load sharing in an autonomous microgrid using supplementary droop control loop," *IEEE Trans. Power Syst.*, vol. 25, no. 2, pp. 796–808, May 2010.
[23] J. M. Guerrero, J. Matas, L. Garcia de Vicuna, M. Castilla, and J. Miret, "Decentralized control for parallel operation of distributed generation inverters using resistive output impedance," *IEEE Trans. Ind. Electron.*, vol. 54, no. 2, pp. 994–1004, Feb. 2007.
[24] Q.-C. Zhong and Y. Zeng, "Universal droop control of inverters with different types of output impedance," *IEEE Access*, vol. 4, pp. 702–712, 2016.
[25] Q.-C. Zhong, "Robust droop controller for accurate proportional load sharing among inverters operated in parallel," *IEEE Trans. Ind. Electron.*, vol. 60, no. 4, pp. 1281–1290, Apr. 2011.
[26] W. Du et al., "A comparative study of two widely used grid-forming droop controls on microgrid small-signal stability," *IEEE Trans. Emerg. Sel. Topics Power Electron.*, vol. 8, no. 2, pp. 963–975, Feb. 2020.
[27] Q. Peng, G. Buticchi, N. M. L. Tan, S. Guenter, J. Yang, and P. Wheeler, "Modeling techniques and stability analysis tools for grid-connected converters," *IEEE Open J. Power Electron.*, vol. 3, pp. 450–467, Dec. 2020.
[28] E. Lenz, D. J. Pagano, A. Ruseler, and M. L. Heldwein, "Two-parameter stability analysis of resistive droop control applied to parallel-connected voltage-source inverters," *IEEE Trans. Emerg. Sel. Topics Power Electron.*, vol. 8, no. 4, pp. 3318–3332, Apr. 2020.
[29] D. Majstorovic, I. Celanovic, N. D. Teslic, N. Celanovic, and V. A. Katic, "Ultralow-latency hardware-in-the-loop platform for rapid validation of power electronics designs," *IEEE Trans. Ind. Electron.*, vol. 58, no. 10, pp. 4708–4716, Oct. 2011.
[30] P. Montero-Robina, K. Rouzbehi, F. Gordillo, and J. Pou, "Grid-following voltage source converters: Basic schemes and current control techniques to operate with unbalanced voltage conditions," *IEEE Open J. Ind. Electron. Soc.*, vol. 2, pp. 528–544, Oct. 2021.
[31] Z. Pan, F. Dong, J. Zhao, L. Wang, H. Wang, and Y. Feng, "Combined resonant controller and two-degree-of-freedom pid controller for PMSLM current harmonics suppression," *IEEE Trans. Ind. Electron.*, vol. 65, no. 9, pp. 7558–7568, Sep. 2018.
[32] T.-L. Lee and S.-H. Hu, "An active filter with resonant current control to suppress harmonic resonance in a distribution power system," *IEEE Trans. Emerg. Sel. Topics Power Electron.*, vol. 4, no. 1, pp. 198–209, Jan. 2016.
[33] S. Fuller, B. Greiner, J. Moore, R. Murray, R. van Paassen, and R. Yorke, "The python control systems library (python-control)," in *Proc. 60th IEEE Conf. Decis. Control*, 2021, pp. 4875–4881.

Eliabe D. Queiroz (Member, IEEE) was born in Mineiros, GO, Brazil, in 1988. He received the B.Sc., M.Sc., and Ph.D. degrees in electrical engineering from the University of Campinas, Campinas, Brazil, in 2015, 2017, and 2023, respectively.

He is currently working on a research and development project in collaboration with the University of Campinas and the Eldorado Research Institute, Campinas, Brazil. His research interests include microgrids, control and synchronization of grid-connected converters, power converters, and electric machine drives.

João I. Y. Ota was born in Sao Paulo, Brazil, in 1985. He received the B.S. and M.S. degrees from the University of Campinas, Campinas, Brazil, in 2009 and 2011, respectively, and the D.Eng. degree from the Tokyo Institute of Technology, Tokyo, Japan, in 2016, all in electrical engineering.

From September 2018 to May 2023, he was a Postdoctoral Researcher with University of Campinas. Since May 2023, he has been an R&D Engineer with Hitachi Energy Sweden AB, Västerås, Sweden. His research interests include microgrids, power quality, and grid-tie power electronics converters such as active harmonic filters, PV inverters, high-power STATCOMs, and battery energy storage systems.

Dr. Ota is a Member of the Brazilian Power Electronics Society. He was a recipient of MEXT Scholarship in 2011–2016.

José Antenor Pomilio (Senior Member, IEEE) was born in Jundiaí, Brazil, in 1960. He received the B.S., M.S., and Ph.D. in electrical engineering from the University of Campinas, Campinas, Brazil, in 1983, 1986, and 1991, respectively.

From 1988 to 1991, he was the Head of the Power Electronics Group, Brazilian Synchrotron Light Laboratory, Campinas, Brazil. He was a visiting Professor with the University of Padova, Padua, Italy, in 1993 and 2015 and with the Third University of Rome, Rome, Italy, in 2003. He is currently a Professor with the School of Electrical and Computer Engineering, University of Campinas, where he has been teaching since 1984. His main interests include power electronics and power quality.

Dr. Pomilio was the President of the Brazilian Power Electronics Society in 2000–2002 and a Member of the Administrative Committee of the IEEE Power Electronics Society in 1997–2002.